Morphology of Porous and Wrinkled Fibers of Polystyrene Electrospun from Dimethylformamide

Chia-Ling Pai,[†] Mary C. Boyce,[‡] and Gregory C. Rutledge*,[†]

Department of Chemical Engineering and Department of Mechanical Engineering, Massachusetts Institute of Technology, 77 Massachusetts Avenue, Cambridge, Massachusetts 02139

Received November 11, 2008; Revised Manuscript Received January 3, 2009

ABSTRACT: Submicron diameter fibers of polystyrene are electrospun from solutions in dimethylformamide (DMF). When electrospun in a high-humidity environment, the interior of these fibers was found to be highly porous rather than consolidated, despite the smooth and nonporous appearance of the fiber surfaces. The formation of interior porosity is attributed to the miscibility of water, a nonsolvent for the polymers in solution, with DMF. The resulting morphology is a consequence of the relatively rapid diffusion of water into the jet, leading to a liquid−liquid phase separation that precedes solidification due to evaporation of DMF from the jet. When electrospun in a low-humidity environment, the fibers exhibit a wrinkled morphology that can be explained by a buckling instability. Understanding which morphology forms under a given set of conditions is achieved through the comparison of three characteristic times: the drying time, the buckling time, and the phase separation time. The morphology has important consequences for the properties of the fibers such as their mechanical strength and stiffness.

Introduction

The basic principle of electrospinning[1−6] is that an electrified jet forms when the free surface of a polymer solution is charged to a high voltage in the presence of an electric field. The jet undergoes continuous stretching as it accelerates downfield toward the collector, thinning further at a very high strain rate (∼1000/s) upon the onset of the whipping instability. Polymer fibers possessing diameters on the order of a few tens or hundreds of nanometers are readily produced by this technology and exhibit specific surface areas on the order of 1−100 m^2/g, much higher than bulk material.

Recently, some remarkable changes in mechanical properties have been reported for electrospun polymeric nanofibers and have been attributed to their small diameters.[7−12] Some researchers have observed the exciting phenomena that polymer fibers with diameters below several hundreds of nanometers have higher moduli[7−10] than the corresponding bulk polymers. Among the possible explanations proposed are supramolecular structure effects[11,12] due to confinement of macromolecular conformation and surface effects[13,14] due to a high ratio of surface area to volume of nanofibers. However, the different morphologies of the fiber that result when processing parameters are changed can also have a significant effect on their properties. Before a comprehensive understanding of the size effect of mechanical properties can be achieved, processing must be controlled in order to eliminate morphological variations that may accompany efforts to produce fibers with different diameters, and the reproducible formation of the desired structures confirmed.

It is well-known[15] that under certain conditions fibers produced by wet or dry spinning techniques can exhibit some porosity. For example, fibers produced by dry spinning typically have a larger internal volume fraction of porosity than those produced by melt spinning. The reason is that melt spinning does not involve a dramatic change in the volume fraction of polymer, while in dry spinning the effect of solvent−polymer interaction and rate of solvent removal need to be considered. Porous surface morphologies[16−20] have been observed in fibers electrospun from solution in a low boiling point solvent; this surface porosity can be varied by controlling the relative humidity of the environment and the molecular weight of the polymer.[16] Kyu and co-workers[21−23] studied the temporal evolution of the fiber morphology theoretically, in the framework of the Cahn−Hilliard phase field approach and the Flory−Huggins free energy of mixing. Their work captures the basic features by which the fiber morphology in a polymer−solvent system undergoing solvent evaporation depends on the competition between the dynamics of phase separation and the rate of solvent evaporation. Their simulations predicted morphologies that ranged from smooth hollow fibers, to fibers with a smooth surface and porous core, to fibers with porous morphologies both at the fiber surface and in the core.[23] The process variables that affect the final fiber morphologies include initial polymer concentration, the rate of solvent evaporation relative to that of phase separation, and temperature. As the polymer concentration of the jet falls into the unstable two-phase region, a slower rate of solvent evaporation relative to that of phase separation, together with a low temperature, promotes the formation of a porous morphology within the fibers.

However, experimental confirmation of electrospun fibers exhibiting a smooth fiber surface and porous interior has not been reported. Such morphologies are easy to overlook by conventional SEM analysis of the fibers, yet will dramatically affect any attempt to rationalize fiber properties. They may be more prevalent than is commonly thought. For these reasons, it is important to understand the conditions under which such morphologies may arise and how they may be recognized. Here, we studied electrospun fibers formed from solutions of amorphous atactic polystyrene (PS) dissolved in a commonly used solvent, dimethylformamide (DMF). Remarkably, we found that fibers with a smooth surface and porous interiors, rather than a homogeneous consolidated solid structure, are readily obtained when the system is electrospun in a very humid environment.

Experimental Section

Materials. Atactic PS (M_w = 280 kg/mol) and dimethylformamide (DMF) (ACS reagent, >99.8%) were purchased from Sigma Aldrich, Inc. Atactic PS (M_w = 2000 kg/mol) was purchased from Scientific Polymer Product Inc. All materials were used without further purification.

* To whom correspondence should be addressed. E-mail: rutledge@mit.edu.
[†] Department of Chemical Engineering.
[‡] Department of Mechanical Engineering.

10.1021/ma802529h CCC: $40.75
Published on Web 02/20/2009

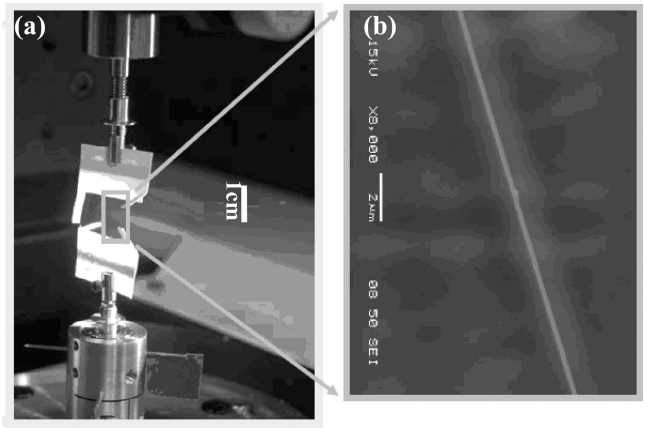

Figure 1. Setup for the uniaxial tensile testing of a single electrospun fiber: (a) a template between two grips (scale bar: 1 cm); (b) a nanofiber between the template (scale bar: 2 μm).

Sample Preparation. A 30 wt % solution of PS (M_w = 280 kg/mol) and 10 wt % solution of PS (M_w = 2000 kg/mol) were dissolved in DMF under gentle stirring for at least 24 h at 50 °C and subsequently cooled down to room temperature before electrospinning. In order to provide a uniform electric field, the parallel-plate electrospinning setup described by Shin et al.[2] was used in our experiments. The flow rate, plate-to-plate distance, and voltage respectively were 0.01 mL/min, 34 cm, and 30 kV for the 30 wt % PS solution and 0.01 mL/min, 34 cm, and 24 kV for the 10 wt % PS solution. In each case, we collected randomly oriented nonwoven meshes on a grounded aluminum foil as well as several single fibers on paper templates. Before characterization, some of the samples of single electrospun PS fibers (with length held fixed when annealed) and of PS mats were annealed at 110 °C for 2 h. The annealing protocol is sufficiently close to the glass transition temperature of the polymer (PS, T_g = 100 °C) and of short duration so that the integrity of the fibers was not compromised. After the heat treatment, all samples were slowly cooled back to room temperature before subsequent analysis.

Characterization. For morphological characterization by scanning electron microscopy (SEM) (JEOL-6060SEM, JEOL Ltd., Japan), fiber samples were sputter-coated with a 3−4 nm layer of gold using a Desk II cold sputter/etch unit (Denton Vacuum LLC). SEM was used to observe the surface structure of fibers at 5 kV acceleration voltage and 15 mm working distance. For observation of interior structures by transmission electron microscopy (TEM) (JEOL JEM200CX TEM, JEOL Ltd., Japan), fibers were embedded in Eponate 12 resin (Ted Pella. Inc.) and cured at 60 °C for 16−24 h. The cross-linked resin was cut into 60 nm slices using a microtome (EM UC6, Leica, Germany) with a diamond blade (DiATOME) and then deposited onto a 300 mesh Cu grid for examination by TEM.

A thermogravimetric analyzer (TGA) (Q50, TA Instruments) was used to determine the content of residual solvent left in the electrospun fibers. Stress−strain curves for single fibers were obtained using the Nano Bionix universal tensile testing system (MTS Systems Corp.), as shown in Figure 1, from which we determined the modulus, tensile strength, and elongation to break of individual electrospun fibers. All uniaxial tensile testing of single electrospun fibers was performed at a strain rate of 10^{-3} s^{-1} and gauge length of 15 mm.

Fiber diameter and void volume fraction inside the fibers were analyzed with the help of AnalySIS image processing software (Soft Imaging System Corp.) and Scion image processing software (National Institutes of Health). The void volume fraction was determined by two methods, from the shrinkage of fiber diameter during annealing and from analysis of TEM images before and after annealing. The values are listed in Table 1. In the first method, the void volume fraction, f_1, was evaluated as $1 - (d_{anneal}^2/d_{as\text{-}spun}^2)$, where $d_{as\text{-}spun}$ is the average diameter of the as-spun fibers and d_{anneal} is the average diameter of the fibers after annealing. This method assumes that the annealed fibers are nonporous, which was confirmed by TEM. Note that annealed fibers and as-spun fibers from the same samples were also used for the tensile testing of single fibers. In the second method for determining void volume fraction, f_2, Scion image processing software was used to set the threshold that distinguishes an image into objects of interest and background on the basis of gray level for the cross-sectional TEM image, and then the area of voids within the fiber can be analyzed. We determine the diameter for each void and the total void volume fraction within the fiber by performing area fraction measurements and comparing the total cross section of voids to that of the fiber. If the voids are sectioned randomly, this void area fraction measurement should provide a reasonable estimate of the true void volume fraction. For fibers electrospun from a 30 wt % PS/DMF solution at 29% relative humidity, the void volume fraction calculated from the shrinkage of fiber diameter and from analysis of TEM images is about 0.5 and 0.3, respectively. The difference between these two analyses can be explained as follows. The accuracy of the void volume fraction from the shrinkage of fiber diameter depends significantly on the standard deviation of fiber diameters. Smaller standard deviation of fiber diameters, which means more uniform fiber diameters, permits a more precise estimation of void volume fraction. Even variations of ±5% in the average of fiber diameter can lead to almost 10% difference in the porosity estimation. As for the TEM image analysis, voids smaller than 10 nm or so are easily overlooked due to the limited resolution and quality of the TEM images. The void volume fraction from TEM images might represent a lower limit of porosity if the grayscale threshold of contrast between the matrix and the void is properly executed. Therefore, each of these analyses yields at best only an approximate estimation of the actual porosity of the fibers.

The cloud point in this study was determined by slowly adding water droplets into the PS/DMF solution until the solution turned turbid. Different concentrations of PS/DMF solutions (5, 10, 15, 20, 25, and 30 wt %) were prepared and tested. Note that local turbidity happened immediately at the interface of the titrated water and the PS/DMF solution; further stirring of the solution for several minutes to a few hours was needed in order to achieve the bulk equilibrium condition. The amount of water was continuously increased, and the solution stirred until the transition from a transparent solution to a turbid solution was observed at equilibrium. The transition was apparent and could be determined by the naked eye without the aid of a spectrophotometer.

Table 1. Diameters of PS Single Fibers

wt %	RH (%)	diameter of as-spun fibers (μm)	diameter of annealed fibers (μm)	f_1 (from the shrinkage of fiber diameter)	f_2 (from analysis of TEM)
30	43	3.93 (±0.42)	2.77 (±0.41)	0.504	0.293
	37	3.57 (±0.32)	2.54 (±0.29)	0.494	0.282
	29	3.52 (±0.22)	2.46 (±0.20)	0.512	0.313
	24	4.09 (±0.30)	2.99 (±0.12)	0.463	0.286
	22	2.96[a]	2.80[a]		
	15	2.51[a,b]	1.80[a,b]		
	11	0.90 (±0.08)[a,b]	0.94 (±0.19)[a,b]		
10	35	2.06 (±0.54)[a]	1.69 (±0.25)[a]	0.328	0.211
	24	1.17 (±0.19)[a]	1.08 (±0.17)[a]	0.147	0.111

[a] Fibers with wrinkled surface. [b] Fibers exhibit beads-on-string morphology.

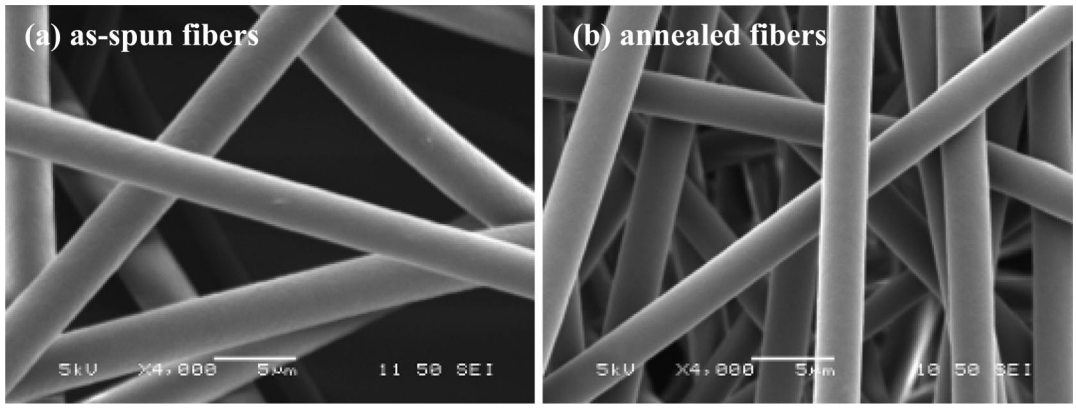

Figure 2. SEM images of fibers electrospun from a 30 wt % PS/DMF solution at 29% relative humidity: (a) as-spun fibers (scale bar: 5 μm); (b) annealed fibers (scale bar: 5 μm).

Results and Discussion

a. Observations of Exterior Fiber Structure before and after Annealing. A 30 wt % solution of PS ($M_w = 280$ kg/mol) dissolved in DMF was electrospun in air at 29% relative humidity and room temperature. As shown in Figure 2a, the as-spun PS fibers have a smooth surface and cylindrical shape. The SEM image shows that the average fiber diameter is 3.52 ± 0.2 μm. After annealing, the morphology shown in Figure 2b is qualitatively similar to the as-spun fibers, but the average fiber diameter is 2.46 ± 0.2 μm, significantly smaller than for the as-spun fibers.

Relative humidity in the environment during fiber spinning affects not only the occurrence of a liquid−liquid phase separation into polymer-rich and polymer-poor regions[16−20] but also the rate of solidification of polymer from either the single-phase or polymer-rich regions.[24] The solidification rate of PS fibers electrospun from DMF is faster at high relative humidity because the water absorbing from the air into the jet acts as a nonsolvent for PS. SEM images of as-spun fibers electrospun from 30 wt % PS/DMF solutions under relative humidity ranging from 11 to 43% are shown in Figure 3. The fibers electrospun at greater than 24% relative humidity have smooth surfaces. Below 24% relative humidity, the smooth surface is replaced by a wrinkled surface, and the fiber diameter tends to be smaller. Table 1 lists the average diameters for as-spun fibers obtained at different relative humidities. Below 15% relative humidity, solidification is delayed to longer time and the jet undergoes further thinning, and eventually capillary instability sets in, resulting in the beads-on-string fiber morphology; both beads and strings exhibit a wrinkled or collapsed surface morphology. The fiber diameter for beads-on-string structures is hard to estimate, particularly for the fiber obtained at 15% relative humidity, near the transition from uniform wrinkled fibers to beads-on-string structures. The average diameter listed in Table 1 merely shows the diameter for strings, not including the beads.

Figure 4 shows SEM images of the same PS fibers as Figure 3, electrospun from 30 wt % PS/DMF solutions under relative humidity ranging from 11 to 43%, after annealing. It shows the alleviation of the wrinkled surface and the shrinkage of fiber diameters when compared with as-spun fibers. This phenomenon indicates that the elimination of wrinkles might be a surface effect. The origin of wrinkles is likely due to buckling of a cylindrical polymer shell under compressive radial stresses, arising from removal of solvent from the core of the jet, and/or a lateral contraction effect from the axial tensile stresses, arising from the continuous stretching of the jet. Annealing permits the fibers to reduce their surface energy by smoothing out the wrinkles and, as shown later, also influences the internal morphology.

b. Mechanical Property Evaluation. Figure 5 shows the engineering stress−engineering strain curves for single PS fibers obtained under uniaxial tension. Each curve is averaged over 15 fibers. Both as-spun and annealed single PS fibers exhibited brittle failure around 2% elongation. However, both the average modulus and ultimate tensile strength were observed to be higher for the annealed fibers. The average modulus and ultimate tensile strength are 1.24 GPa and 17 MPa for as-spun fibers and 3.57 GPa and 49 MPa for annealed fibers. For purposes of comparison, a cast PS film of thickness 74.4 ± 4.2 μm exhibited average modulus and ultimate tensile strength of 3.63 GPa and 43 MPa after annealing. Literature values for modulus and ultimate tensile strength for bulk PS are around 3.0−3.6 GPa and 40−60 MPa, respectively.[25,26] Thus, both the annealed fibers and the film exhibit mechanical properties comparable to bulk PS. One possible speculation for the inferior mechanical performance of as-spun single fibers is that some residual solvent was retained in the as-spun fibers due to the high boiling point (153 °C) of DMF. However, thermogravimetric analysis results (not shown) indicated less than 5% weight loss around the boiling point of DMF for electrospun mats stored at room temperature for 24 h prior to the testing. Such a low level of residual DMF would not account for the poorer mechanical properties of the as-spun fibers. An alternative explanation is that the fibers differ in their internal morphologies; this possibility is examined in the next section.

c. Observation of Interior Fiber Structure. Figure 6a shows a cross-sectional TEM image of as-spun PS fibers. The TEM image clearly reveals the presence of large voids within the interior of the fiber. The void volume fraction obtained from image analysis is about 30%; the voids range in diameter from 10 to 300 nm. Analysis of images of numerous fibers indicates that whereas the void volume fraction is relatively constant, the void sizes can vary dramatically from fiber to fiber. Voids as large as 700 nm were observed in fibers of diameter 3.52 μm. The presence of voids would lower the modulus and strength of the fiber and would serve as points of stress concentration during tensile testing. By contrast, no obviously visible voids are observed in the annealed PS fibers (Figure 6b). Note that annealing fibers at a temperature above T_g resulted in a smooth surface and a consolidated interior; in contrast, annealing fibers at 65 °C under vacuum for 24 h does not eliminate the interior porous structure, as shown in Figure 7. Therefore, careful annealing of the fibers at a temperature just slightly above the glass transition temperature seems to be an effective way to achieve interior solid structure.

d. Rationalization of Interior and Exterior Structure in Terms of Models. The formation of surface pores has been attributed on different occasions to phase separation[16−20] and to "breath figures" resulting from water condensation on the surface of the liquid jet.[16,17,27−29] Rabolt and co-workers demonstrated that porous surface features on fibers electrospun from low

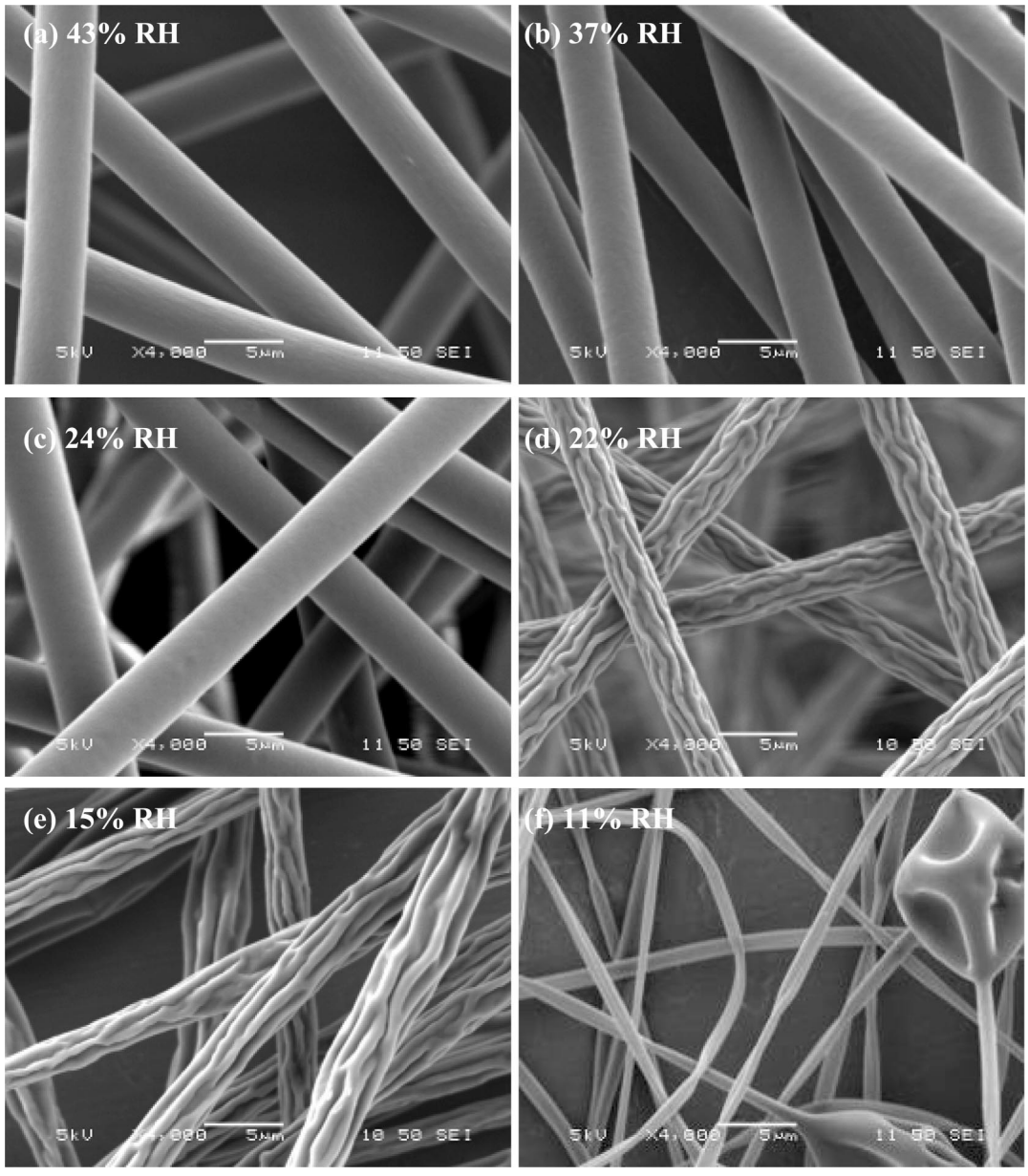

Figure 3. SEM images of as-spun fibers electrospun from a 30 wt % PS/DMF solution under (a) 43%, (b) 37%, (c) 24%, (d) 22%, (e) 15%, and (f) 11% relative humidity (scale bar: 5 μm).

boiling point solvent can be varied by controlling the relative humidity of the surrounding air and the molecular weight of the polymer.[16,17] The dependence of pore size on polymer molecular weight suggests that phase separation is the governing mechanism in this case. A liquid−liquid phase separation occurs via spinodal decomposition and/or nucleation and growth. The polymer-rich phase solidifies and the solvent-rich phase leads ultimately to the formation of pores. During electrospinning, the most relevant phase separation processes are thermally induced phase separation (TIPS), attributed to the rapid evaporation of solvent that lowers the temperature on the fiber surface, and vapor-induced phase separation (VIPS), associated with water vapor in the surrounding air that acts as the nonsolvent. In our PS/DMF system, most fibers electrospun from the high boiling point DMF were without surface pores. It indicates that TIPS and breath figures are not contributing mechanisms in our case because the evaporation of DMF is slow compared to a low boiling solvent such as tetrahydrofuran (THF); it is unlikely to decrease the temperature on the fiber surface to a value low enough either to bring about TIPS or to condense water. In the PS/DMF system, VIPS may be responsible for the production of porous structures within the fibers. Given the miscibility of water with DMF, the water from the humid environment may be absorbed into the jet and play a role as nonsolvent for PS; VIPS then precedes solidification due to the slow evaporation rate of DMF. To understand this behavior, one needs to consider a ternary composition of H_2O/DMF/PS in the jet. A ternary phase diagram for H_2O/DMF/PS was constructed in this study based on the Flory−Huggins theory.[30] The mass transfer of the three components during the fiber formation was then calculated for representative operating conditions, and the resulting mass transfer paths were superposed onto the ternary phase diagram.[31−33]

For a ternary mixture, the Gibbs free energy of mixing can be expressed as

$$\frac{\Delta G_M}{RT} = n_1 \ln \varphi_1 + n_2 \ln \varphi_2 + n_3 \ln \varphi_3 + g_{12}(u_2) n_1 \varphi_2 + g_{13}(\varphi_3) n_1 \varphi_3 + g_{23}(\varphi_3) n_2 \varphi_3 \quad (1)$$

Subscripts 1, 2, and 3 refer to nonsolvent (H_2O), solvent (DMF), and polymer (PS), respectively. R is the gas constant, and T is the

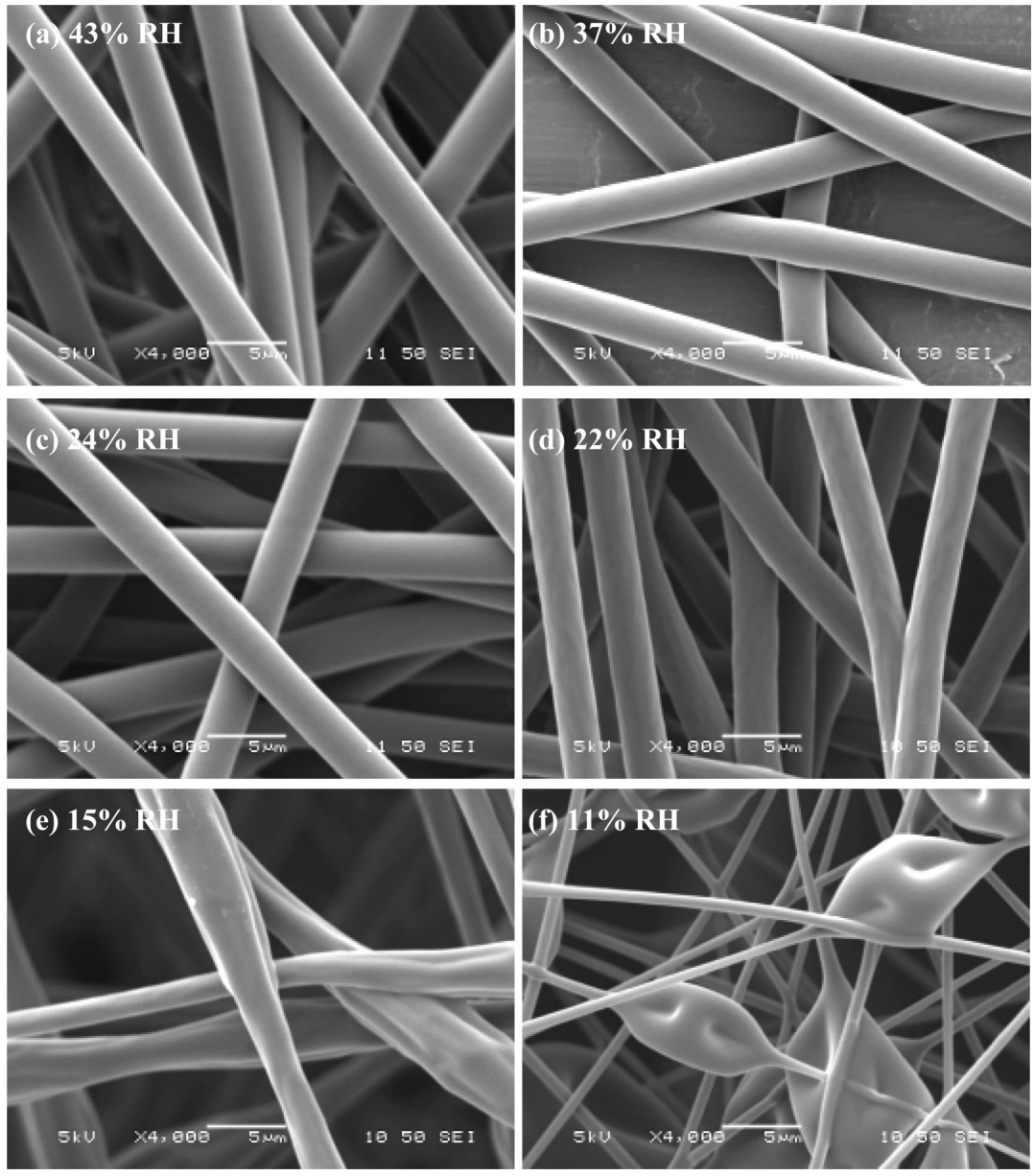

Figure 4. SEM images of annealed fibers electrospun from a 30 wt % PS/DMF solution under (a) 43%, (b) 37%, (c) 24%, (d) 22%, (e) 15%, and (f) 11% relative humidity (scale bar: 5 μm).

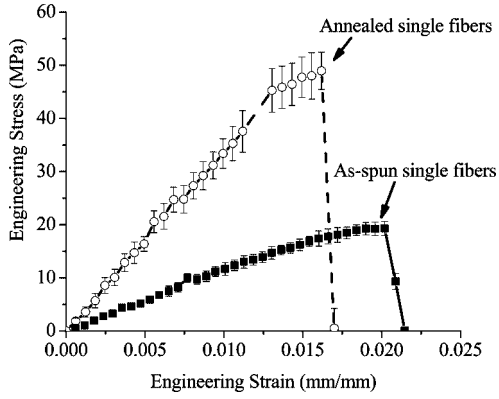

Figure 5. Engineering stress−strain curves for single fibers electrospun from a 30 wt % PS/DMF solution at 29% relative humidity. Each datum is averaged over 15 fibers, and error bars correspond to 1 standard deviation.

absolute temperature; n_i and φ_i are the number of moles and the volume fraction of component i; g_{ij} is the concentration-dependent interaction parameter between component i and j. g_{12} is expressed as a function of u_2, where $u_2 = \varphi_2/(\varphi_1 + \varphi_2)$, and g_{13} and g_{23} are both functions of φ_3.

The chemical potential of component i is given by μ_i, and $\Delta\mu_i$ is the chemical potential difference between component i and its pure liquid state at the same temperature,[30] where $\Delta\mu_i/RT = (\partial(\Delta G_M/RT)/\partial n_i)_{n_{j\neq i}}$. The chemical potential difference for each component can be expressed as

$$\frac{\Delta\mu_1}{RT} = \ln\varphi_1 + 1 - \varphi_1 - \frac{v_1}{v_2}\varphi_2 - \frac{v_1}{v_3}\varphi_3 + (g_{12}\varphi_2 + g_{13}\varphi_3)(\varphi_2 + \varphi_3) - g_{23}\frac{v_1}{v_2}\varphi_2\varphi_3 - (1 - u_2)u_2\varphi_2\left(\frac{dg_{12}}{du_2}\right) - \varphi_1\varphi_3^2\left(\frac{dg_{13}}{d\varphi_3}\right) - \frac{v_1}{v_2}\varphi_2\varphi_3^2\left(\frac{dg_{23}}{d\varphi_3}\right) \quad (2)$$

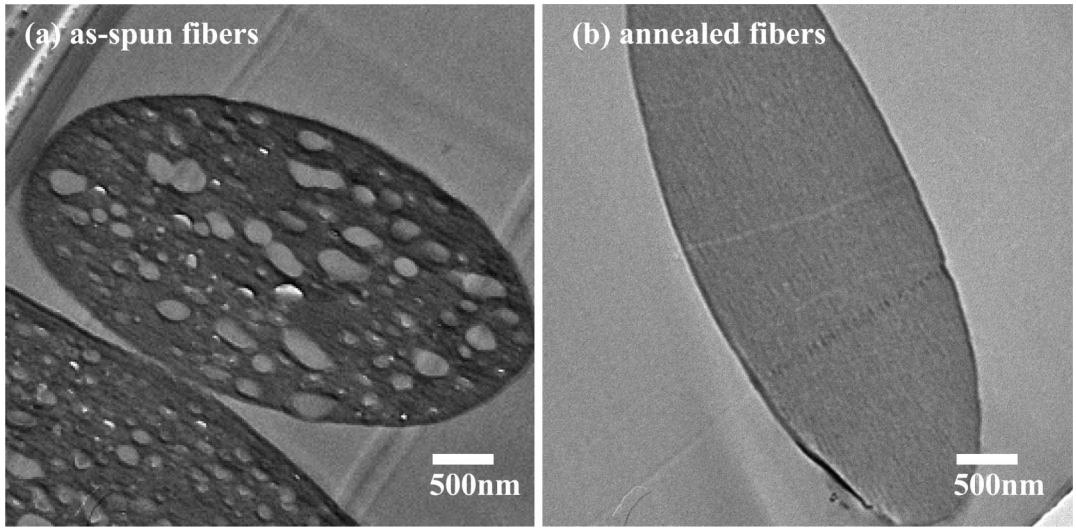

Figure 6. Cross-sectional TEM images of fibers electrospun from a 30 wt % PS/DMF solution at 29% relative humidity: (a) as-spun fibers (scale bar: 500 nm); (b) annealed fibers (scale bar: 500 nm). The elliptic cross section of the fiber is an artifact of cutting the sample at an oblique angle.

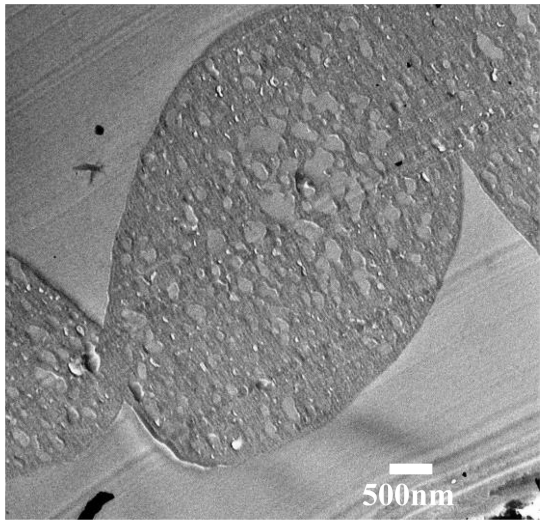

Figure 7. Cross-sectional TEM image of fibers electrospun from a 30 wt % PS/DMF solution at 29% relative humidity and then annealed at 65 °C under vacuum for a day (scale bar: 500 nm).

$$\frac{\Delta\mu_2}{RT} = \ln\varphi_2 + 1 - \varphi_2 - \frac{v_2}{v_1}\varphi_1 - \frac{v_2}{v_3}\varphi_3 + \left(g_{12}\frac{v_2}{v_1}\varphi_1 + g_{23}\varphi_3\right)(\varphi_1 + \varphi_3) - g_{13}\frac{v_2}{v_1}\varphi_1\varphi_3 + (1 - u_2)u_2\frac{v_2}{v_1}\varphi_1\left(\frac{\mathrm{d}g_{12}}{\mathrm{d}u_2}\right) - \frac{v_2}{v_1}\varphi_1\varphi_3{}^2\left(\frac{\mathrm{d}g_{13}}{\mathrm{d}\varphi_3}\right) - \varphi_2\varphi_3{}^2\left(\frac{\mathrm{d}g_{23}}{\mathrm{d}\varphi_3}\right) \quad (3)$$

$$\frac{\Delta\mu_3}{RT} = \ln\varphi_3 + 1 - \varphi_3 - \frac{v_3}{v_1}\varphi_1 - \frac{v_3}{v_2}\varphi_2 + \left(g_{13}\frac{v_3}{v_1}\varphi_1 + g_{23}\frac{v_3}{v_2}\varphi_2\right)(\varphi_1 + \varphi_2) - g_{12}\frac{v_3}{v_1}\varphi_1\varphi_2 + \left[\frac{v_3}{v_1}\varphi_1\left(\frac{\mathrm{d}g_{13}}{\mathrm{d}\varphi_3}\right) + \frac{v_3}{v_2}\varphi_2\left(\frac{\mathrm{d}g_{23}}{\mathrm{d}\varphi_3}\right)\right]\varphi_3(\varphi_1 + \varphi_2) \quad (4)$$

$v_i$represents the molar volume of pure species *i*. The binodal curve can be calculated from the equality of the chemical potential between the polymer-rich (A) and polymer-lean (B) phases.

$$\Delta\mu_{i,\mathrm{A}} = \Delta\mu_{i,\mathrm{B}} \quad (i = 1, 2, 3) \quad (5)$$

The spinodal curve can be calculated from the following equation:[34]

$$G_{22}G_{33} = (G_{23})^2 \quad (6)$$

where $G_{ij} = (\partial^2\overline{\Delta G_{\mathrm{M}}}/(\partial\varphi_i\ \partial\varphi_j))v_{\mathrm{ref}}$, $\overline{\Delta G_{\mathrm{M}}}$ is the Gibbs free energy of mixing per unit volume, and v_{ref} is the molar volume of the reference component, which is component 1 in this study.

An expression for g_{12} for the DMF/water system was reported by Altena et al.:[35]

$$g_{12}(u_2) = 0.50 + 0.04u_2 + 0.8u_2{}^2 - 1.20u_2{}^3 + 0.8u_2{}^4 \quad (7)$$

Following the studies of Matsuyama et al. and Yip et al., we assumed constant values for g_{13} and g_{23} in our work.[32,33] The solvent−polymer interaction parameter g_{23} for DMF/PS can be roughly estimated by[36]

$$g_{23} = 0.34 + \frac{v_2(\delta_2 - \delta_3)^2}{RT} \quad (8)$$

δ_i is the solubility parameter for component *i* ($\delta_{\mathrm{DMF}} = 24.8$ $(\mathrm{MPa})^{1/2}$ and $\delta_{\mathrm{PS}} = 22.49$ $(\mathrm{MPa})^{1/2}$).[36,37] The calculated value of $g_{23} = 0.506$ is similar to the experimental data ($g_{23} = 0.497$) from Wolf et al.[38] The latter was used here. The nonsolvent−polymer interaction parameter g_{13} is generally estimated from the swelling experiment; however, no experimental data for an H_2O/PS system could be found in the literature. Therefore, g_{13} was treated as a fitting parameter in our study. It was found that the calculated binodal curve fits the cloud point curve well by setting $g_{13} = 2.2$, as shown in Figure 8. The parameters used to construct the ternary phase diagram for the H_2O/DMF/PS system are listed in Table 2.

To determine mass transfer pathways, radial diffusion within a fiber with negligible end effects was modeled; the geometry for the system is shown in Figure 9. The diffusion equations are

$$\frac{\partial\varphi_1}{\partial t} = \frac{1}{r}\frac{\partial}{\partial r}\left(rD_{11}\frac{\partial\varphi_1}{\partial r} + rD_{12}\frac{V_1}{V_2}\frac{\partial\varphi_2}{\partial r}\right) \quad (9)$$

Table 2. Parameters Used To Construct the Ternary Phase Diagram

ν_1 (cm^3/mol)	18.0
ν_2 (cm^3/mol)	77.4
ν_3 (cm^3/mol)	266667
g_{13}	2.2
g_{23}	0.497

$$\frac{\partial \varphi_2}{\partial t} = \frac{1}{r}\frac{\partial}{\partial r}\left(rD_{21}\frac{V_2}{V_1}\frac{\partial \varphi_1}{\partial r} + rD_{22}\frac{\partial \varphi_2}{\partial r}\right) \tag{10}$$

where D_{ij} is the appropriate phenomenological diffusion coefficient, r is the radial direction in cylindrical coordinates, and V_i is the partial specific volume of component i in the fiber. Because φ_1 is much smaller than φ_2, the quasi-binary system was substituted for eq 10, giving

$$\frac{\partial \varphi_2}{\partial t} = \frac{1}{r}\frac{\partial}{\partial r}\left(rD_2\frac{\partial \varphi_2}{\partial r}\right) \tag{10'}$$

where D_2 is the mutual diffusion coefficient of the solvent in the binary system. Initial conditions and boundary conditions for eqs 9 and 10′are

$$t = 0: \qquad \varphi_1 = \varphi_{10}, \quad \varphi_2 = \varphi_{20} \tag{11}$$

$$r = 0: \qquad \frac{\partial \varphi_1}{\partial r} = \frac{\partial \varphi_2}{\partial r} = 0 \tag{12}$$

$$r = R(t) \qquad -D_{11}\frac{\partial \varphi_1}{\partial r} - D_{12}\frac{V_1}{V_2}\frac{\partial \varphi_2}{\partial r} = k_1 V_1(\rho_{1g}^i - \rho_{1g}^{inf})$$
$$-D_2\frac{\partial \varphi_2}{\partial r} = k_2 V_2(\rho_{2g}^i - \rho_{2g}^{inf}) \tag{13}$$

Subscript 0 refers to the initial condition. $R(t)$ is the fiber radius at time t, k_i is the gas-side mass transfer coefficient of component i, and ρ_{ig} is the mass density of component i in the gas phase. Superscripts i and inf refer to the air−fiber interface and in the bulk gas phase, respectively. Because this is a moving boundary problem, η was defined here to simplify the problem and facilitate the calculation by finite differences:

$$\eta = \frac{r}{R(t)} \tag{14}$$

Also, because of the difficulties of direct stability analysis,[31] diffusion coefficients were assumed to be independent of η. In this form, the diffusion equations, initial conditions, and boundary conditions are

$$\left(\frac{\partial \varphi_1}{\partial t}\right)_\eta = \frac{\eta}{R(t)}\frac{dR(t)}{dt}\frac{\partial \varphi_1}{\partial \eta} + \frac{D_{11}}{\eta R(t)^2}\frac{\partial \varphi_1}{\partial \eta} + \frac{D_{12}}{\eta R(t)^2}\frac{V_1}{V_2}\frac{\partial \varphi_2}{\partial \eta} + \frac{D_{11}}{R(t)^2}\frac{\partial^2 \varphi_1}{\partial \eta^2} + \frac{D_{12}}{R(t)^2}\frac{V_1}{V_2}\frac{\partial^2 \varphi_2}{\partial \eta^2} \tag{15}$$

$$\left(\frac{\partial \varphi_2}{\partial t}\right)_\eta = \frac{\eta}{R(t)}\frac{dR(t)}{dt}\frac{\partial \varphi_2}{\partial \eta} + \frac{D_2}{\eta R(t)^2}\frac{\partial \varphi_2}{\partial \eta} + \frac{D_2}{R(t)^2}\frac{\partial^2 \varphi_2}{\partial \eta^2} \tag{16}$$

$$t = 0: \qquad \varphi_1 = \varphi_{10}, \quad \varphi_2 = \varphi_{20} \tag{17}$$

$$\eta = 0: \qquad \frac{\partial \varphi_1}{\partial \eta} = \frac{\partial \varphi_2}{\partial \eta} = 0 \tag{18}$$

$$\eta = 1 \qquad -D_{11}\frac{\partial \varphi_1}{\partial \eta} - D_{12}\frac{V_1}{V_2}\frac{\partial \varphi_2}{\partial \eta} = k_1 R(t) V_1(\rho_{1g}^i - \rho_{1g}^{inf})$$
$$-D_2\frac{\partial \varphi_2}{\partial \eta} = k_2 R(t) V_2(\rho_{2g}^i - \rho_{2g}^{inf}) \tag{19}$$

$$R(t) = \left(\frac{\pi R_0^2 \varphi_{30}}{\int_0^1 2\pi\eta\varphi_3\, d\eta}\right)^{1/2} \tag{20}$$

The equations for determining the diffusion coefficients and mass transfer coefficients are listed in the Appendix. Finite differences for one-dimensional and time-dependent partial differential equations (15) and (16) were performed using Matlab (R2008a, The Mathworks Inc.). All the parameters used for the mass transfer calculation are listed in Table 3.

Figure 8 shows the calculated ternary phase diagram for our system and the mass transfer paths for 30 wt % PS/DMF solutions jetted under conditions of different relative humidity. Once the water was transported into the system, phase separation occurred almost instantly (within 1 s) for high relative humidity, ranging from 30% (0.57 s) to 50% (0.18 s). It is apparent from Figure 8 that at low relative humidity (10% and 20%) it was relatively hard to induce phase separation. Note that DMF is a very common solvent used to dissolve various polymers for use in electrospinning; therefore, it is perhaps not surprising that several authors have noted the sensitivity of fiber formation to the relative humidity of the surrounding air.[39,40] The possible porous structure within as-spun fibers can be the result of water vapor in the environment acting as nonsolvent. In order to obtain homogeneous solid fibers, careful consideration should be paid to the proper selection of solvent, the environmental factors, and the need of postspinning heat treatment.

Figure 10 shows TEM images of cross sections of as-spun fibers electrospun from a 30 wt % PS/DMF solution at different relative humidities. Obvious porous structures within the fiber were observed for fibers electrospun from high relative humidity ranging from 24 to 43%. For as-spun fibers obtained at low

Table 3. Parameters Used in Mass Transfer Calculation

w_{10}	10^{-20}	M_1 (g/mol)	18	R (erg/(mol K))	8.314×10^7
w_{20}	0.7	M_2 (g/mol)	73.09	T (K)	300
w_{30}	0.3	M_3 (g/mol)	280 000	N_A	6.022×10^{23}
ρ_1 (g/cm^3)	1.00	K_{22}/γ (cm^3/(g K))	9.76×10^{-4}	R_0 (cm)	5×10^{-4}
ρ_2 (g/cm^3)	0.94	$K_{32} - T_{g2}$ (K)	−43.8	ξ (−)	0.47
ρ_3 (g/cm^3)	1.05	K_{23}/γ (cm^3/(g K))	5.82×10^{-4}	D_{20} (cm^2/s)	8.48×10^{-4}
V_1 (cm^3/g)	1.00	$K_{33} - T_{g23}$ (K)	−327	$D^{12}(\varphi_1 = 1)$ (cm^2/s)	1.12×10^{-5}
V_2 (cm^3/g)	1.06	P_1^0 (atm)	0.0313	D_{1g} (cm^2/s)	0.267
V_3 (cm^3/g)	0.95	P_2^0 (atm)	4.79×10^{-3}	D_{2g} (cm^2/s)	0.023
V_2* (cm^3/g)	0.926	P_t (atm)	1	μ_g (g/(cm s))	1.85×10^{-4}
V_3* (cm^3/g)	0.850	ρ_{1g}^{inf} (g/cm^3)	humidity[a]	ρ_g (g/cm^3)	1.18×10^{-3}
V_{1g} (cm^3/g)	1358	ρ_{2g}^{inf} (g/cm^3)	10^{-20}	τ_1^d (−)	0.413
V_{2g} (cm^3/g)	335	D_c (cm)	10×10^{-4}	τ_2^d (−)	−1.65

[a] $\rho_{1g}^{inf} = 2.715 \times 10^{-5} \times$ (RH) g/cm^3.

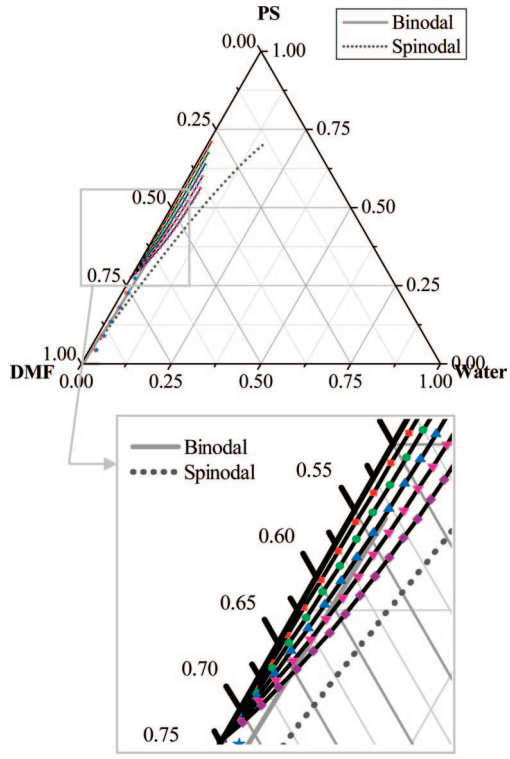

Figure 8. Ternary phase diagram for the three-component system. Experimental data: (red star symbol: before observed cloud point; blue star symbol: after observed cloud point). Theoretical binodal (solid gray curve) and spinodal (dotted curve). Theoretical mass transfer paths for 30 wt % PS/DMF solutions (■, 10%; ●, 20%; ▲, 30%; ▼, 40%; ♦, 50% relative humidity). Each data point represents an interval of 0.05 s.

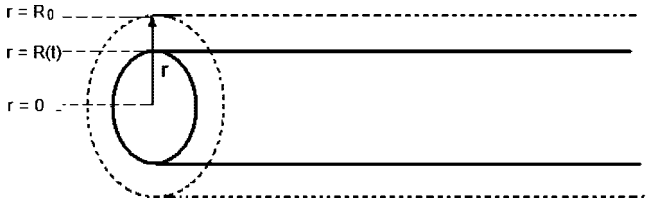

Figure 9. Geometry for the mass transfer calculation.

relative humidity, having wrinkled or collapsed structures, only a few, small voids were observed in Figure 10d−f. Note that the larger cross section of the fiber in Figure 10e,f corresponds to the beads, and the smaller cross sections correspond to the strings. Our calculated results for the ternary phase diagram and the mass transfer path predict the occurrence of phase separation within the fibers for different relative humidities in this experiment. Figure 11 shows the elimination of interior voids within the annealed PS fibers; one observes the same phenomenon as described in Figure 6b. Both are probably driven by the thermodynamic tendency to eliminate high-energy surfaces. It is interesting to observe that the void volume fraction is far less for the slightly collapsed fiber with wrinkled surface and severely collapsed fiber with ribbonlike morphology than for circular and smooth fibers. In order to understand this phenomenon, the reason why these wrinkled and collapsed fiber structures were formed should also be understood; this is discussed next.

e. Fiber Morphological Evolution. Khoombungse et al. have reported[41] that electrospun fibers with typical diameters larger than 1 μm can adopt a variety of cross-sectional shapes, including flat ribbons and wrinkled surfaces. They postulated that the thin skin layer initially formed on polymer fibers as the solvent evaporates tends to collapse under atmospheric pressure. This is a well-known buckling instability.[42,43] Pauchard et al.[44−46] have also observed such a phenomenon for evaporation of solvent from a sessile drop of polymer solution. Once the buckling instability occurs, complex spatial and temporal evolutions lead to unexpected collapsed shapes of the drops, which are qualitatively similar to the collapsed electrospun fiber, in particular, the beads. The key to understanding this buckling instability is the formation of a glassy skin on the drop (or fiber) surface. In their analysis, Pauchard et al.[44] identified two characteristic times, the drying time t_D and the buckling time t_B, and give an order of magnitude description of both:

$$t_D = \frac{V_0}{S_0 W_{E0}} = \frac{R_0}{2W_{E0}} \tag{21}$$

$$t_B = \frac{D_2(\varphi_{pg} - \varphi_{p0})^2}{W_{E0}^2} \tag{22}$$

where V_0 is the initial volume, S_0 is the initial vapor/drop surface area, R_0 is the initial radius of the fiber, W_{E0} is the initial evaporation rate, D_2 is the mutual diffusion coefficient for the solvent−polymer system, φ_{pg} is the polymer volume fraction at the drop surface undergoing vitrification, and φ_{p0} is the polymer volume fraction in the core of the drop. According to Pauchard et al., if t_B is smaller than t_D, the buckling instability may be observed. The general idea of these two characteristic times, t_B and t_D, can be used here to predict whether the fibers will collapse or not under certain conditions, for instance, different evaporation rates or solidification rates, polymer concentrations, or molecular weights of the polymer.

Figure 12shows the proposed fiber cross sections for morphological evolution of the structures. These can be classified into two groups: one without phase separation (in which the polymer solidifies into a surface skin layer) and the other with phase separation (within the fibers, leading to a porous network interior). For the first four morphologies in Figure 12a−d, no phase separation occurs. For example, PS/DMF solutions electrospun at extremely low relative humidity experience little absorption of water from the vapor into the system, so that liquid−liquid phase separation from VIPS is unimportant. Another example is from the work done by Rabolt and co-workers.[16,17] In their PS/THF system, all of the fibers have a collapsed ribbonlike shape because the evaporation of THF precedes the diffusion of water from the vapor into the fiber. Therefore, only the characteristic times of t_B and the drying time t_D should be considered here. If t_B is larger than t_D, the morphology should resemble that shown in Figure 12a. If t_B is smaller than t_D, the morphology should resemble that shown in Figure 12d. If t_B is comparable to t_D, the morphology falls between (b) and (c) of Figure 12. The difference between (b), (c), and (d) depends on the mode number of the dominant buckling instability around the fiber circumference.[43] The determination of the dominant mode number depends on the skin thickness and modulus as well as the modulus of the internal core; the skin thickness in turn depends on how much skin forms prior to buckling and is related to the ratio t_B/t_D. Many factors influence the magnitudes of t_B and t_D. Generally, larger fibers tend to collapse due to the longer drying time that accompanies the reduced surface area for evaporation of solvent; polymer solution made from higher molecular weight polymer tends to collapse due to the shorter buckling time that results from a smaller mutual diffusion coefficient; and polymer solution of larger concentration tends to collapse due to the smaller difference between the polymer concentration at the fiber surface and in the core of the fiber.

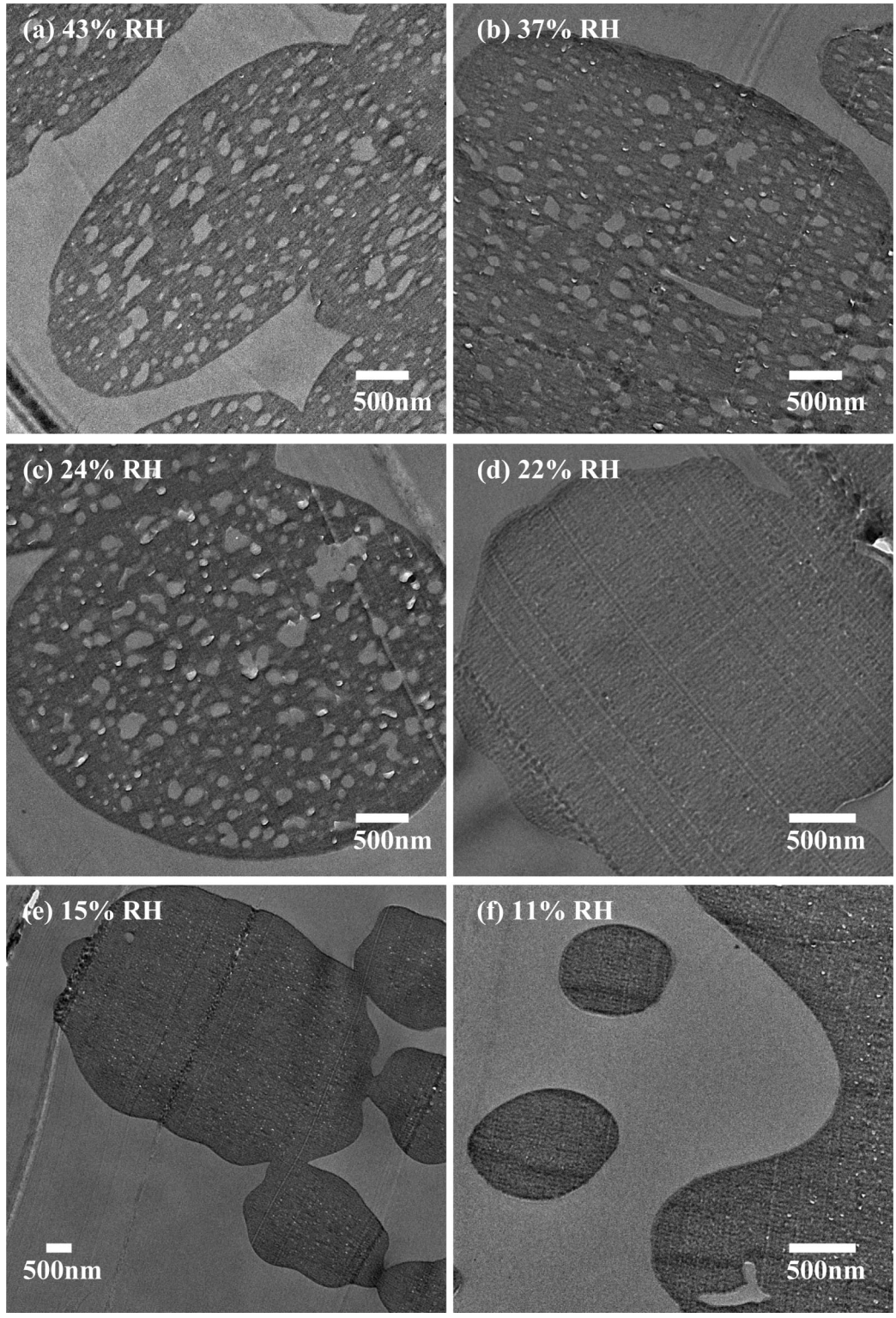

Figure 10. Cross-sectional TEM images of as-spun fibers electrospun from a 30 wt % PS/DMF solution under (a) 43%, (b) 37%, (c) 24%, (d) 22%, (e) 15%, and (f) 11% relative humidity (scale bar: 500 nm).

However, in our PS/DMF system, the fiber morphology evolution is closer to those shown in Figure 12e−h. As mentioned before, water vapor acts like a nonsolvent for PS, and it is miscible with DMF. Here, the phase separation rate is faster than the evaporation rate of the high boiling DMF, and it helps to alleviate the occurrence of buckling, especially when electrospinning is performed under a very humid environment. With the uptake of water from the vapor as a nonsolvent for the polymer, the thin skin formed on the fiber surface does not collapse as easily as the one without the phase separation. Therefore, besides the characteristic times for t_B and t_D, another characteristic time should be considered here, which is the characteristic time for phase separation, t_{PS}. For that reason, by controlling the nature of the operating environment, such as the relative humidity, and the fluid properties, such as polymer−solvent interaction, combined with the concentration of polymer and the molecular weight of polymer, the morphology can be manipulated between Figure 12e−h. Note that the void volume

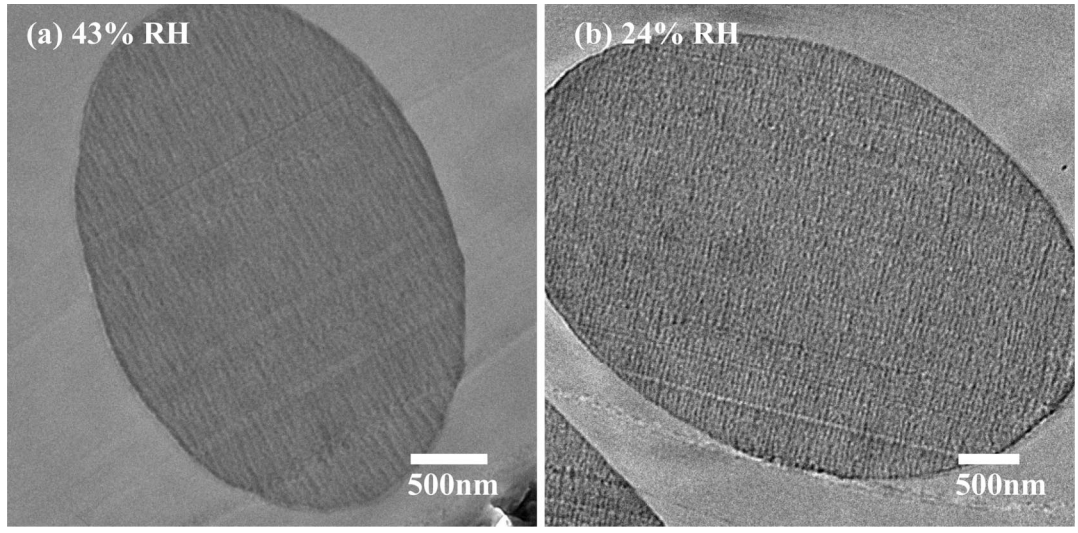

Figure 11. Cross-sectional TEM images of annealed fibers electrospun from a 30 wt % PS/DMF solution under (a) 43% and (b) 24% relative humidity (scale bar: 500 nm).

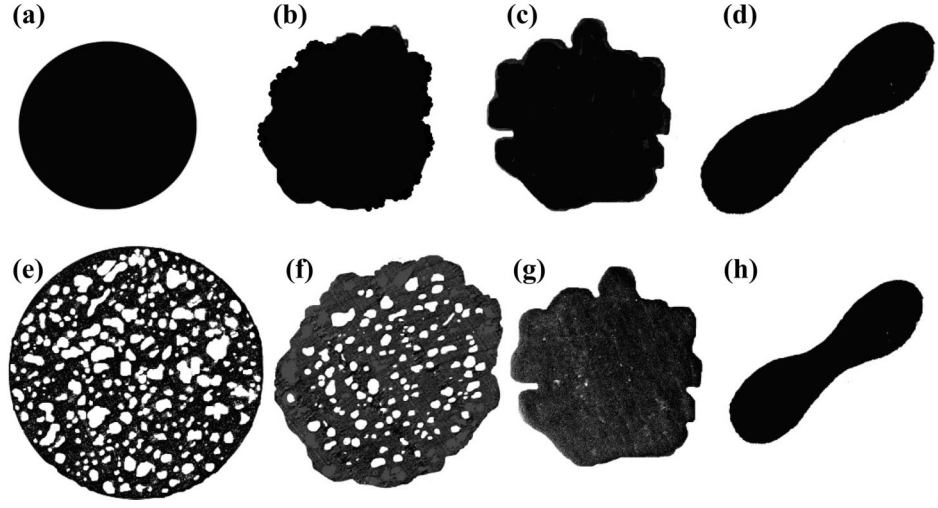

Figure 12. Proposed fiber cross sections for morphology evolution. Two groups: one without phase separation, from (a) through (d), and the other with phase separation, from (e) through (h).

Table 4. Comparison for Different Time Scales[a]

RH (%)	W_{E0} (μm/s)	time for phase separation, t_{ps} (s)	drying time from eq *21*, t_D (s)	bucking time from eq *22*, t_B (s)
10	3.228	N/A	0.774	0.490
20	3.016	N/A	0.829	0.561
30	2.774	0.57	0.901	0.663
40	2.510	0.28	0.996	0.810
50	2.227	0.18	1.123	1.029

[a] D_2 (2×10^{-7} cm^2/s), W_{E0}, and t_{PS} were obtained from the mass transfer calculation.

fraction and void size differ with different levels of the collapse. The maximum void volume fraction that can be sustained inside the fiber should be a function of the material stiffness. Table 4 shows rough estimates of the time for phase separation (based on the time to reach the intersection of the operating pathway and the binodal in Figure 8), the drying time (from eq 21), and the buckling time (from eq 22) in our system. R_0 was roughly estimated to be 5 μm, derived from the observed as-spun fiber diameter and the original concentration of polymer in solution. Note the value of φ_{pg} was unknown and had to be assumed here; the buckling time varies significantly with changes of φ_{pg}. A value for φ_{pg} of 0.78 performs reasonably well to describe our observations, but further investigation should be done in the future. In our calculation listed in Table 4, $t_{PS}/t_B < 1$ indicates the smooth appearance of fibers electrospun from high relative humidity (from 30 to 50%) because phase separation precedes buckling instability, giving rise to an interior pore network that prevents buckling. For $t_{PS}/t_B > 1$ and $t_{PS}/t_D > 1$, the competition between buckling and drying dominates the resulting morphology; under these circumstances, $t_D/t_B > 1$ (applicable to all the cases observed in this work) indicates the formation of a wrinkled surface, consistent with the observed morphology of fibers electrospun from low relative humidity (10 and 20%), because the buckling instability precedes both phase separation and solvent drying. The time scales for the phase separation, solvent drying, and buckling instability in our system are very similar and fall between 0.1 and 1.2 s.

In order to demonstrate further the occurrence of buckling instability, a 10 wt % solution of higher molecular weight PS ($M_w = 2000$ kg/mol) dissolved in DMF was electrospun at room temperature and at both 35 and 24% relative humidity. SEM images in Figure 13 show the surface wrinkled morphology of as-spun and annealed fibers. Compared with the fibers shown in Figure 3 obtained at the same relative humidities, the collapsed structures are apparently obtained more readily for the fibers made from the polymer with high molecular weight. This accords with eq 22. Since D_2 decreases with increasing

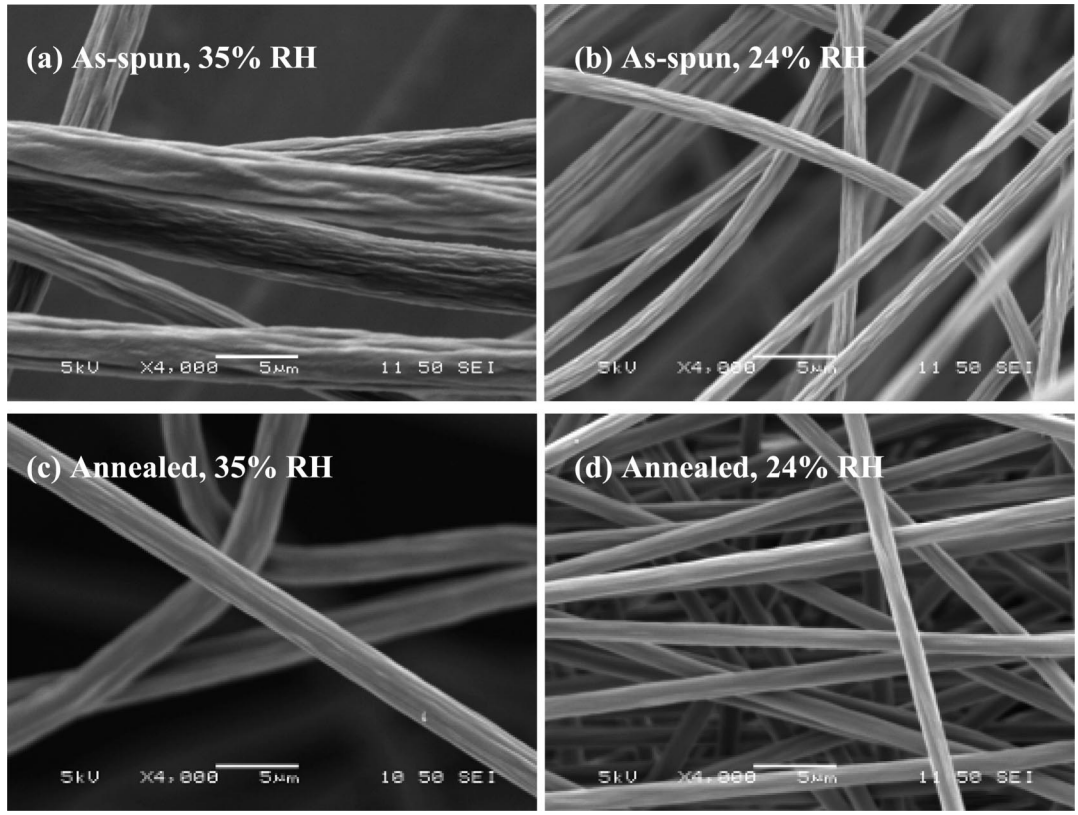

Figure 13. SEM images of as-spun fibers electrospun from a 10 wt % PS/DMF solution under (a) 35% and (b) 24% relative humidity (scale bar: 5 μm) and annealed ones from (c) 35% and (d) 24% relative humidity (scale bar: 5 μm).

molecular weight, t_B is shorter and the buckling instability is favored. Figure 14 shows TEM cross-section images of as-spun and annealed fibers. Porous structures within the fiber were observed, but with less void volume fraction for the as-spun fiber due to the collapsed structures.

Lastly, as evidence for the generality of these phenomena, we report qualitatively similar behavior for fibers of polyacrylonitrile (PAN, M_w =150 kg/mol) electrospun from solutions of 11−14 wt % polymer in DMF and 30−50% relative humidity. Processing at the higher relative humidity or lower polymer concentration produces smooth fibers, whose diameters decrease upon annealing. At the lower relative humidity and higher polymer concentration, wrinkled fibers are found, indicative of the buckling instability. These trends are consistent with those observed for the PS/DMF system. In this case, the void sizes in the porous fibers are smaller than in the PS/DMF system and harder to quantify, and changes in properties upon annealing are further complicated by the semicrystalline nature of PAN. A detailed analysis of these materials will be reported subsequently.

Conclusion

Porous structures within fibers were found in a PS/DMF system electrospun in a humid environment. Because DMF is a commonly used solvent in electrospinning, the possible occurrence of this phenomenon may be more prevalent than has been appreciated to date and may also occur for other similar polymer−solvent systems. The reason for porous structures to occur within fibers is because the humidity in the environment plays a role as nonsolvent. For the miscibility of water with DMF, liquid-induced phase separation precedes solidification due to the slow evaporation rate of DMF. The formation of porous features within the fibers has a significant effect on the mechanical performance. Other properties such as optical properties and electrical properties may be altered with different porosity, void sizes, void shapes, and their distribution inside the fibers. By controlling the environmental factors (such as relative humidity, temperature, and surrounding gas composition), the polymer−solvent interaction, the concentration of polymer, and the molecular weight of polymer, either porous or homogeneous solid fibers, can be produced and manipulated in accord with the needs of specific applications, such as sensors, membranes in solar cells, filtration, drug delivery, catalytic systems, hydrogen storage systems, protective clothing with breathability and toxic chemical resistance, and tissue engineering. For example, porous fibers can be considered a composite material composed of polymer and air. Depending on the volume fraction and distribution of pores, the gas permeability through the fiber is different, which can be used to advantage for gas separation or to enhance the breathability of a material. For the collapsed structures such as those observed in Figure 10d, the shape is excellent for enhancing the oleophobic or hydrophobic nature of the nonwoven material because the second, finer scale of roughness associated with wrinkling is more resistant to wetting. Also, some of our collapsed fiber geometries are similar to the capillary surface materials with surfaces engineered to contain deep grooves, which can act as capillary channels or fluid conduits. The phenomenal absorbency of these fibers can be used in liquid chromatography.

Appendix

The diffusion coefficients, D_2,[47−50] D_{11}, and D_{12},[31,53] were estimated based on the following equations and are functions of φ.

where D_2* is the self-diffusion coefficient of the solvent. D_{20} is the pre-exponential factor of the solvent.[50] E is the energy per mole for a molecule to overcome attractive forces from its neighbors and was assumed to be zero here.[50] V_i* is the specific critical hole

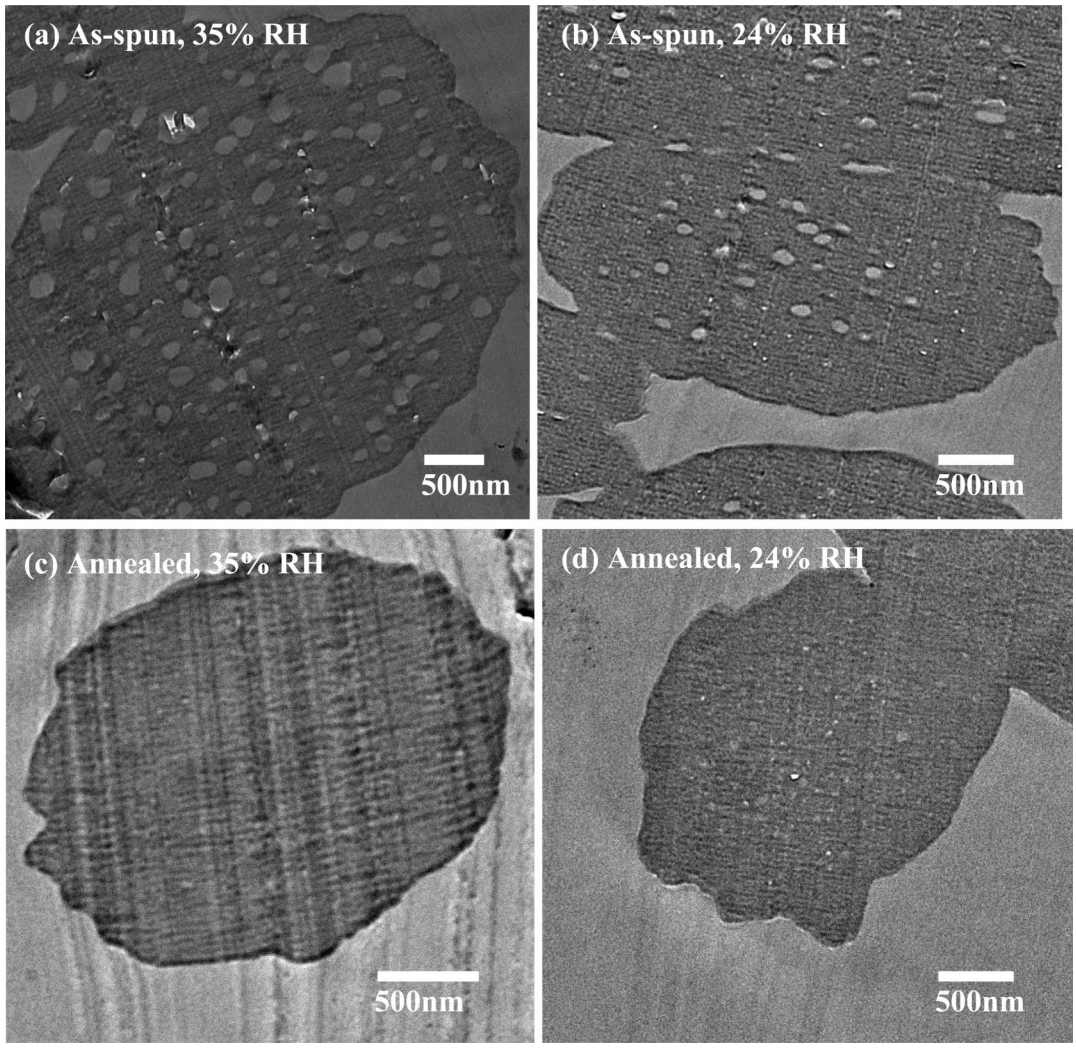

Figure 14. Cross-sectional TEM images of as-spun fibers electrospun from a 10 wt % PS/DMF solution under (a) 35% and (b) 24% relative humidity (scale bar: 500 nm) and annealed ones from (c) 35% and (d) 24% relative humidity (scale bar: 500 nm).

free volume required for a jump for component i.[50,52] w_i is the weight fraction of component i. ξ is the ratio of molar volumes for the solvent and polymer jumping units.[50] K_{22}, K_{32}, K_{23}, and K_{33} are free volume parameters.[50] γ is the overlap factor.[50] T_{gi} is the glass transition temperature of component i.[50] N_A is Avogadro's number. M_i is the molecular weight of component i. ζ_{12}, ζ_{23}, and ζ_{13} are the friction parameters.[51] D^{12} is the mutual diffusion coefficient in solvent−nonsolvent system.[53]

The gas-side mass transfer coefficient k_i for single horizontal cylinders under free convection is[54]

$$D_2^* = D_{20}\mathrm{e}^{-E/RT} \exp\left(-\frac{w_2V_2^* + w_3\xi V_3^*}{w_2(K_{22}/\gamma)(K_{32} - T_{g2} + T) + w_3(K_{23}/\gamma)(K_{33} - T_{g3} + T)}\right) \quad (23)$$

$$D_2 = D_2^*(1 - \varphi_2)^2(1 - 2g_{23}\varphi_2) \quad (24)$$

$$D_{11} = -\frac{V_1}{{N_A}^2E_0}\left(E_{22}\frac{\partial\mu_1}{\partial\varphi_1} - E_{12}\frac{\partial\mu_2}{\partial\varphi_1}\right) \quad (25)$$

$$D_{12} = -\frac{V_2}{{N_A}^2E_0}\left(E_{22}\frac{\partial\mu_1}{\partial\varphi_2} - E_{12}\frac{\partial\mu_2}{\partial\varphi_2}\right) \quad (26)$$

$$E_{12} = \frac{(1 - \varphi_1)\zeta_{12}}{M_2\varphi_3} - \frac{RTV_2}{{N_A}^2D_{T1}\varphi_3} \quad (27)$$

$$E_{22} = \frac{V_2\varphi_1\zeta_{12}}{v_1\varphi_3} - \frac{RTV_2(1 - \varphi_1)}{{N_A}^2D_{T2}\varphi_2\varphi_3} \quad (28)$$

$$E_0 = -\frac{{\zeta_{12}}^2}{M_1M_2\varphi_3} + \frac{R^2T^2V_1V_2}{{N_A}^4D_{T1}D_{T2}\varphi_1\varphi_2\varphi_3} \quad (29)$$

$$D_{T1} = \frac{RT}{{N_A}^2(\varphi_2\zeta_{12}/v_2 + \varphi_3\zeta_{13}/v_3)} \quad (30)$$

$$D_{T2} = \frac{RT}{{N_A}^2(\varphi_1\zeta_{12}/v_1 + \varphi_3\zeta_{23}/v_3)} \quad (31)$$

$$\zeta_{12} = \frac{v_1RT}{{N_A}^2D^{12}(\varphi_1 = 1)} \quad (32)$$

$$\zeta_{23} = \frac{v_3RT}{{N_A}^2D_2^*\varphi_3} \quad (33)$$

$$\zeta_{13} = 0.5(v_1/v_2)\zeta_{23} \quad (34)$$

$$k_i = \frac{0.53(Gr_i Sc_i)^{0.25} D_{ig}}{D_c y_{air}^{lm}} \quad (35)$$

$$Gr_i = \frac{D_c^3 \rho_g^2 g}{\mu_g^2} |\tau_i (y_{ig}^i - y_{ig}^{inf})| \quad (36)$$

$$Sc_i = \frac{\mu_g}{\rho_g D_{ig}} \quad (37)$$

where D_c is the characteristic diameter of the fiber. y_{air}^{lm} is the logarithmic mean of y_{ig}^i and y_{ig}^{inf}. D_{ig},[55,56] ρ_g,[57] and μ_g[57] are the mutual diffusion coefficient of component i in the gas phase, total mass density of the gas phase, and viscosity of the gas, respectively. y_{ig} are the mole fraction of component i. g is the gravitational constant. τ_i is calculated from $-1/\rho_g(\partial\rho_g/\partial y_{ig})_{P,T}$.

ρ_{ig}^i was calculated by

$$\rho_{ig}^i = a_i P_i^0/(V_{ig} P_t) \quad (38)$$

$$a_i = \exp(\Delta\mu_i/RT) \quad (39)$$

where a_i is the activity of component i. P_t and P_i^0[55,58] are the total pressure and the saturated vapor pressure for pure component i. V_{ig} is the partial specific volume of component i in the gas phase. The detailed derivation for mass transfer equations is presented in refs 31−33.

Acknowledgment. We thank Dr. Steven Kooi and Dr. Cheng-Yen Wen for help with the initial setup of the nano tensile tester and for discussion of mechanical measurement, Dr. Jian H. Yu for his expertise in electrospinning, Dr. Yeo-Wan Chiang and Dr. Minglin Ma for the helpful discussions of TEM sample preparation, and Dr. Pradipto K. Battarcharjee for the discussion of general electrospinning issues. This research was supported by the U.S. Army through the Institute for Soldier Nanotechnologies (ISN) under Contract DAAD-19-02-D-0002 with the U.S. Army Research Office.

References and Notes

(1) Hohman, M. M.; Shin, M.; Rutledge, G. C.; Brenner, M. P. *Phys. Fluids* **2001**, *13*, 2201–2220.
(2) Hohman, M. M.; Shin, M.; Rutledge, G. C.; Brenner, M. P. *Phys. Fluids* **2001**, *13*, 2221–2236.
(3) Yu, J. H.; Fridrikh, S. V.; Rutledge, G. C. *Polymer* **2006**, *47*, 4789–4797.
(4) Reneker, D. H.; Yarin, A. L.; Fong, H.; Koombhongse, S. *J. Appl. Phys.* **2000**, *87*, 4531–4547.
(5) Rutledge, G. C.; Fridrikh, S. V. *Adv. Drug Delivery Rev.* **2007**, *59*, 1384–1391.
(6) Dzenis, Y. *Science* **2004**, *304*, 1917–1919.
(7) Ji, Y.; Li, B. Q.; Ge, S. R.; Sokolov, J. C.; Rafailovich, M. H. *Langmuir* **2006**, *22*, 1321–1328.
(8) Chew, S. Y.; Hufnagel, T. C.; Lim, C. T.; Leong, K. W. *Nanotechnology* **2006**, *17*, 3880–3891.
(9) Lee, S. H.; Tekmen, C.; Sigmund, W. M. *Mater. Sci. Eng., A* **2005**, *398*, 77–81.
(10) Li, L.; Bellan, L. M.; Craighead, H. G.; Frey, M. W. *Polymer* **2006**, *47*, 6208.
(11) Shin, M. K.; Kim, S. I.; Kim, S. J.; Kim, S. K.; Lee, H.; Spinks, G. M. *Appl. Phys. Lett.* **2006**, *89*, 231929.
(12) Arinstein, A.; Burman, M.; Gendelman, O.; Zussman, E. *Nat. Nanotechnol.* **2007**, *2*, 59–62.
(13) Cuenot, S.; Frétigny, C.; Demoustier-Champagne, S.; Bernard, N. *Phys. Rev. B* **2004**, *69*, 165410.
(14) Dingreville, R.; Qu, J. M.; Cherkaoui, M. *J. Mech. Phys. Solids* **2005**, *53*, 1827–1854.
(15) Statton, W. O. *J. Polym. Sci.* **1962**, *58*, 205–220.
(16) Casper, C. L.; Stephens, J. S.; Tassi, N. G.; Chase, D. B.; Rabolt, J. F. *Macromolecules* **2004**, *37*, 573–578.
(17) Megelski, S.; Stephens, J. S.; Chase, D. B.; Rabolt, J. F. *Macromolecules* **2002**, *35*, 8456–8466.
(18) Bognitzki, M.; Czado, W.; Frese, T.; Schaper, A.; Hellwig, M.; Steinhart, M.; Greiner, A.; Wendorff, J. H. *Adv. Mater.* **2001**, *13*, 70–72.
(19) Jeun, J. P.; Kim, Y. H.; Lim, Y. M.; Choi, J. H.; Jung, C. H.; Kang, P. H.; Nho, Y. C. *J. Ind. Eng. Chem.* **2007**, *13*, 592–596.
(20) Miyauchi, Y.; Ding, B.; Shiratori, S. *Nanotechnology* **2006**, *17*, 5151–5156.
(21) Dayal, P.; Kyu, T. *J. Appl. Phys.* **2006**, *100*, 043512.
(22) Guenthner, A. J.; Khombhongse, S.; Liu, W. X.; Dayal, P.; Reneker, D. H.; Kyu, T. *Macromol. Theory Simul.* **2006**, *15*, 87–93.
(23) Dayal, P.; Liu, J.; Kumar, S.; Kyu, T. *Macromolecules* **2007**, *40*, 7689–7694.
(24) Tripatanasuwan, S.; Zhong, Z. X.; Reneker, D. H. *Polymer* **2007**, *48*, 5742–5746.
(25) Mathur, D.; Nauman, E. B. *J. Appl. Polym. Sci.* **1999**, *72*, 1165–1176.
(26) Yokouchi, M.; Seto, S.; Kobayashi, Y. *J. Appl. Polym. Sci.* **1983**, *28*, 2209–2216.
(27) Srinivasarao, M.; Collings, D.; Philips, A.; Patel, S. *Science* **2001**, *292*, 79–83.
(28) Reneker, D. H.; Chun, I. *Nanotechnology* **1996**, *7*, 216–223.
(29) Limaye, A. V.; Narhe, R. D.; Dhote, A. M.; Ogale, S. B. *Phys. Rev. Lett.* **1996**, *76*, 3762.
(30) Yilmaz, L.; McHugh, A. J. *J. Appl. Polym. Sci.* **1986**, *31*, 997–1018.
(31) Tsay, C. S.; McHugh, A. J. *J. Polym. Sci., Part B: Polym. Phys.* **1990**, *28*, 1327–1365.
(32) Matsuyama, H.; Teramoto, M.; Nakatani, R.; Maki, T. *J. Appl. Polym. Sci.* **1999**, *74*, 159–170.
(33) Yip, Y.; McHugh, A. J. *J. Membr. Sci.* **2006**, *271*, 163–176.
(34) Tompa, H. *Polymer Solutions*; Butterworths: London, 1956; p 46.
(35) Altena, F. W.; Smolders, C. A. *Macromolecules* **1982**, *15*, 1491–1497.
(36) Brandrup, J.; Immergut, E. H.; Grulke, E. A.; Abe, A.; Bloch, D. R. *Polymer Handbook*, 4th ed.; Wiley-Interscience: New York, 1999.
(37) Burke, J. *Solubility Parameters: Theory and Application, AIC Book and Paper Group Annual* **1984**, *3*, 13–58.
(38) Wolf, B. A.; Willms, M. M. *Makromol. Chem.* **1978**, *179*, 2265–2277.
(39) Kongkhlang, T.; Kotaki, M.; Kousaka, Y.; Umemura, T.; Nakaya, D.; Chirachanchai, S. *Macromolecules* **2008**, *41*, 4746–4752.
(40) Mattoso, L. H. C.; Offeman, R. D.; Wood, D. F.; Orts, W. J.; Medeiros, E. S. *Can. J. Chem. Rev. Can. Chim* **2008**, *86*, 590–599.
(41) Koombhongse, S.; Liu, W. X.; Reneker, D. H. *J. Polym. Sci., Part B: Polym. Phys.* **2001**, *39*, 2598–2606.
(42) Timoshenko, S. P.; Gere, J. M. *Theory of Elastic Stability*, 2nd ed.; McGraw-Hill: New York, 1961.
(43) Flügge, W. *Stresses in Shells*, 2nd ed.; Springer: New York, 1973.
(44) Pauchard, L.; Hulin, J. P.; Allain, C. *Europhys. News* **2005**, *36*, 9–11.
(45) Pauchard, L.; Allain, C. *Europhys. Lett.* **2003**, *62*, 897–903.
(46) Pauchard, L.; Couder, Y. *Europhys. Lett.* **2004**, *66*, 667–673.
(47) Vrentas, J. S.; Duda, J. L. *AIChE J.* **1979**, *25*, 1–24.
(48) Vrentas, J. S.; Duda, J. L.; Ling, H. C. *J. Polym. Sci., Polym. Phys. Ed.* **1984**, *22*, 459–469.
(49) Duda, J. L.; Ni, Y. C.; Vrentas, J. S. *Macromolecules* **1979**, *12*, 459–462.
(50) Zielinski, J. M.; Duda, J. L. *AIChE J.* **1992**, *38*, 405–415.
(51) Vrentas, J. S.; Duda, J. L.; Ling, H. C. *J. Appl. Polym. Sci.* **1985**, *30*, 4499–4516.
(52) Sugden, S. *J. Chem. Soc.* **1927**, 1786–1798.
(53) Wilke, C. R.; Chang, P. *AIChE J.* **1955**, *1*, 264–270.
(54) McAdams, W. H. *Heat Transmission*, 3rd ed.; McGraw-Hill: New York, 1954; p 177.
(55) The Society of Chemical Engineers of Japan, Ed.; *Handbook of Chemical Engineering* (in Japanese), 5th ed.; Maruzen: Tokyo, 1988.
(56) Bird, R. B.; Stewart, W. E.; Lightfoot, E. N. *Transport Phenomena*; John Wiley & Sons: New York, 1960.
(57) Lide, D. R. *Handbook of Chemistry and Physics*, 71st ed.; CRC Press: Boca Raton, FL, 1990.
(58) The Chemical Society of Japan, Ed.; *Handbook of Chemistry* (in Japanese), 4th ed.; Maruzen: Tokyo, 1993.

MA802529H